Polarimetric SAR Interferometry Forest Height Inversion Error Model: The Impact of the Nonideal System Parameters

Zenghui Huang, Xiaolei Lv, *Member, IEEE*, and Xiaoshuai Li

***Abstract*—The model-based polarimetric interferometric synthetic aperture radar forest height inversion is inherently affected by nonideal system parameters, including channel imbalance, crosstalk, and noise. To investigate the impact of nonideal system parameters on the estimated forest height, this article introduces an analytical forest height inversion error model based on the two-layer randomly oriented volume over ground model. First, the error transfer function is derived to present the forest height error caused by the disturbance of the volume coherence. Then, the coupled effects of the nonideal system parameters on the volume coherence are established and demonstrated to reduce the amplitude of the volume coherence. The effects of channel imbalance and crosstalk are explicitly derived and found to be coupled together to amplify the noise. Finally, the error model is established by combining the error transfer function and the disturbance of the volume coherence caused by the nonideal system parameters. The proposed error model is verified by simulation analyses on real airborne repeat-pass BioSAR 2008 datasets. The results demonstrate that the proposed model can accurately capture the relationship between the height estimation errors and the system parameters.**

***Index Terms*—Error model, forest height inversion, polarimetric interferometric synthetic aperture radar (PolInSAR), polarimetric system parameter.**

I. Introduction

FOREST height is a pivotal biophysical parameter in biomass estimation, forest management, biodiversity, and global carbon storage. In recent decades, polarimetric interferometric synthetic aperture radar (PolInSAR) has shown great potential in forest height and biomass estimation [1], [2], [3]. Extensive research has demonstrated that the forest height can be estimated from PolInSAR data at X-, C-, L-, and P-bands for different stands and terrain conditions [4], [5], [6], [7], [8].

Manuscript received 19 January 2024; revised 11 March 2024; accepted 1 May 2024. Date of publication 8 May 2024; date of current version 30 May 2024. This work was supported by the LuTan-1 L-Band Spaceborne Bistatic SAR data processing program under Grant E0H2080702. *(Corresponding author: Xiaolei Lv.)*

The authors are with the Key Laboratory of Technology in Geo-spatial Information Processing and Application System, Aerospace Information Research Institute, Chinese Academy of Sciences, Beijing 100190, China, also with the Aerospace Information Research Institute, Chinese Academy of Sciences, Beijing 100094, China, and also with the School of Electronic, Electrical, and Communication Engineering, University of Chinese Academy of Sciences, Beijing 100049, China (e-mail: huangzenghui20@mails.ucas.ac.cn; academism2017@sina.com; lixiaoshuai21@mails.ucas.ac.cn).

Digital Object Identifier 10.1109/JSTARS.2024.3398009

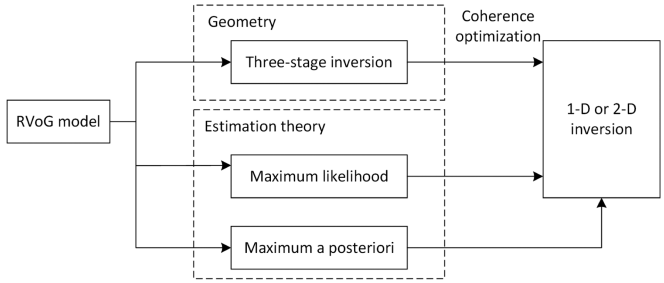

Fig. 1. Inversion methods under the RVoG framework.

The random volume over ground (RVoG) model is widely used in forest height inversion due to its balanced tradeoff between physical structure and model complexity [9], [10]. Many inversion methods have been established under the framework of this two-layer model as shown in Fig. 1. The three-stage inversion (TSI) process was proposed according to the geometrical characteristics of the RVoG model [11]. Some coherence optimization methods have been studied to reduce the contribution of ground scattering in the volume coherence [12], [13]. Nevertheless, the geometry-based methods lack quantitative evaluation on the estimation of ground and volume coherence despite the explicit physical meaning. The maximum likelihood (ML) inversion was derived from the aspect of estimation theory to optimally recover the canopy structural parameters [14]. However, its objective function often exhibits two indistinguishable peaks that correspond to the candidates of the ground phase in the TSI. It inevitably makes the inversion ill-posed. Then, the maximum a posteriori (MAP) inversion was proposed to solve the double-candidate effect of the ground phase in the ML method [15]. Some researchers have investigated reducing temporal correlation based on the RVoG model but increased the complexity of the model, leading to a multidimensional optimization problem [16], [17]. Some nonparametric inference methods are presented to estimate the forest height based on machine learning and deep learning [18], [19], [20], and the performance of these algorithms highly depends on the training samples.

As PolInSAR technology is rapidly advancing, the availability and diversity of PolInSAR systems are steadily increasing. Several onboard SAR satellites, such as the L-band SAOCOM satellite series [21], [22], the Terrain Wide-Swath Interferometric L-Band SAR mission [23] have provided lots of quad-polarization images with different spatial and temporal baselines

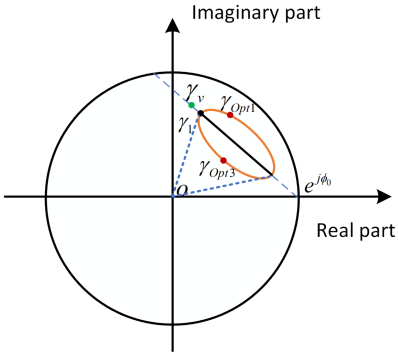

Fig. 2. Geometric interpretation of the RVoG model in the unit circle; orange ellipse: coherence region; green dot: volume coherence; black dot: candidate of the volume coherence; red dots: Lagrange-optimized coherences; solid black line: line fitted through coherence region.

for extracting the forest structure information. Furthermore, the European Space Agency and German Aerospace Center plan to launch the BIOMASS mission [24] and Tandem-L mission [25] in 2024, respectively.

Given the increasing availability of polarization systems and data, there is an urgent need to comprehensively investigate the impact of these system parameters on the results and to develop effective systematic error correction strategies. For system designers, it is crucial to understand how to achieve a balance among different system parameters while meeting specific accuracy requirements.

Most of the studies in the literature concentrated on the forest height model to improve the accuracy and efficiency of the inversion [10], [13], [26]. However, the forest height estimation is inherently affected by various nonideal system parameters, including channel imbalance, crosstalk, noise, and other perturbations. Few studies are concerned with the forest height estimation errors caused by the nonideal system parameters [27], [28]. Cloude [27] studied the effects of polarimetric calibration errors on the performance of model-based height estimation using PolInSAR and concluded that the optimum coherence remains invariant to the calibration errors under a high signal-to-noise ratio (SNR). Wang and Xu [28] considered the effects of crosstalk, channel imbalance, and noise, and proposed a forest height error model by integrating the Lagrange coherence optimization [29] and phase-amplitude joint method [30] (referred to as LPA). However, the Lagrange-optimized coherences used in LPA usually do not lie in the main direction of the coherence region, as shown in Fig. 2. It may cause the inversion heights to be seriously overestimated or underestimated and thus influence the accuracy of the error model. The error model considered crosstalk and channel imbalance separately, which in fact coupled with each other. In addition, the approximation in the model introduced an additional hyperparameter that needed to be adjusted, making the generalization challenging.

This study aims to establish an error model to present the impacts of the nonideal system parameters on the estimated forest height for the most widely used RVoG-based methods, including TSI, ML, and MAP, as shown in Fig. 1. To facilitate the analysis, the formulation is based on the TSI method. First, the error transfer function is derived according to the Taylor series approximation of the sinc function. It presents the forest height error caused by the disturbance of the volume coherence. Then, based on the phase diversity method [12], the coupled effects of channel imbalance, crosstalk, and noise on the volume coherence are analyzed. Combined with the error transfer function, the height estimation error model is explicitly derived as a multivariate function involving six physical parameters: channel imbalance, vertical and horizontal crosstalks, SNR, volume coherence, and vertical wavenumber. Finally, the applicability of the model for other configurations is discussed. The proposed error model cannot only serve as a valuable reference for system designers in determining system parameters with specific accuracy requirements but also provide a systematic error correction strategy. Compared with the LPA model, the proposed model relies on fewer assumptions and has better performance and generalization.

The rest of this article is organized as follows. Section II presents the RVoG-based TSI scheme and the error transfer function. Section III introduces the model assumptions and the influence of channel imbalance, crosstalk, and noise on the polarimetric coherency and interferometry matrix. Further, the error model between the polarimetric system parameters and the height estimation errors is presented by analyzing the impact of nonideal system parameters on volume coherence. In Section IV, the experiments are performed on real airborne SAR data to verify the proposed error model. Section V discusses how to design the PolInSAR system parameters and correct the systematic errors according to the error model. In addition, it presents the model applicability analysis and limitations. Finally, Section VI concludes this article.

II. Model-Based PolInSAR Inversion

A. PolInSAR Parameter Inversion

Under the two-layer assumption, the RVoG model formulates the complex interferometric coherence $\gamma(\vec{\mathbf{w}})$ as [10]

$$\gamma(\vec{\mathbf{w}}) = e^{j\phi_0}\frac{\gamma_v + \mu(\vec{\mathbf{w}})}{1+\mu(\vec{\mathbf{w}})} \tag{1}$$

where ϕ_0 is the ground phase, γ_v is the volume coherence, the unitary complex projection vector $\vec{\mathbf{w}}$ denotes the corresponding polarization channel, and the ground-to-volume scattering ratio μ [11]. For the scatterers with an exponential decay vertical structure function [31], the volume coherence can be formulated as a ratio of integrals [8], [9]

$$\gamma_v(h_v, k_e) = \frac{\int_0^{h_v} e^{\frac{2k_e z}{\cos\theta}} e^{jk_z z} dz}{\int_0^{h_v} e^{\frac{2k_e z}{\cos\theta}} dz} \tag{2}$$

where k_e indicates the mean extinction coefficient, h_v denotes the forest height, and the vertical wavenumber k_z [10]

$$k_z = \frac{4\pi}{\lambda}\frac{B_\perp}{R\sin(\theta-\alpha)} \tag{3}$$

where θ is the incidence angle, α is the local terrain slope, $B_\perp$ is the perpendicular baseline, R denotes the slant range distance, and λ is the wavelength.

Fig. 2 presents the geometric interpretation of the RVoG model. In the RVoG model (1), the interferometric coherence

is a linear combination of the volume and ground coherences. Thus, the coherence region is a straight-line segment whose length, location, and orientation depend on the acquisition parameters, scattering parameters, and systematic errors. However, the deviations from the underlying RVoG model assumptions and the uncertainties in the coherence estimation introduce a more ellipse-like shaped coherence region rather than a straight line segment [32].

The volume coherence γ_v and ground phase ϕ_0 can be estimated by employing the coherence loci [11], [26]. In this study, the volume coherence is estimated according to the phase diversity method [12]. Then, two remaining parameters, height, and extinction can be retrieved to minimize the difference between the model predictions and observations [11]

$$(\tilde{h}_v, \tilde{k}_e) = \arg\min_{h_v, k_e} |\gamma_v e^{-j\phi_0} - \gamma_v(h_v, k_e)| \tag{4}$$

where (h_v, k_e) is the grid point on a 2-D precalculated look-up table, $(\tilde{h}_v, \tilde{k}_e)$ presents the estimated height and extinction.

Compared with the comprehensive RVoG inversion in (4), there exists a more efficient and robust alternative method [3], [8], [30], which fixes the extinction value as $k_e = 0$ as suggested in [5] and [8]. In this case, the volume coherence in (2) becomes

$$\gamma_v(h_v) = \exp\left(j\frac{k_z h_v}{2}\right)\operatorname{sinc}\left(\frac{k_z h_v}{2}\right) \tag{5}$$

where $\operatorname{sinc}(x) = \sin(x)/x$. Then, the inversion can be done only using the amplitude of the coherence as

$$h_v = \frac{2\operatorname{sinc}^{-1}(|\gamma_v|)}{k_z}. \tag{6}$$

Note that although the 2-D look-up table is reduced to 1-D using simplification, the volume coherence is estimated by the coherence loci optimization as mentioned above.

B. Error Transfer Function

According to (6), the channel imbalance, crosstalk, and noise will influence the final inversion results by disturbing the amplitude of the volume coherence. Therefore, we need to find out the following relationship:

$$\Delta h_v = g\left(k_z, \Delta|\gamma_v|\right). \tag{7}$$

The above relationship is solved as long as the inverse of the sinc function is derived. Due to the ambiguity height, the estimation in (6) only considers the interval of $[0, \pi]$. However, the sinc function does not have an analytic inverse function. Applying the Taylor series to the sinc function yields

$$y = 1 - \frac{x^2}{3!} + \frac{x^4}{5!} - \frac{x^6}{7!} + \frac{x^8}{9!} + o[x]^{10}. \tag{8}$$

Fig. 3 shows the approximation error curves of the sinc function and its Taylor polynomial of different degrees in the full inversion interval of $[0, \pi]$. Obviously, the higher the series order, the smaller the approximation error. The error between the sinc function and its Taylor polynomial of degree 8 in (8) is less than $x^{10}/11!$. In the range of $[0, \pi]$, the error is no more than 0.0022, which is negligible.

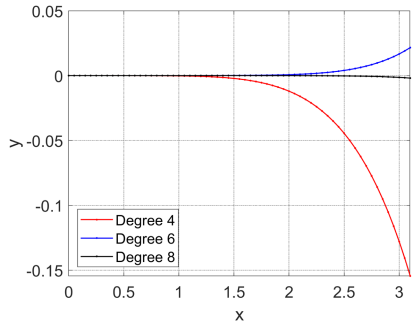

Fig. 3. Approximation error curves between sinc function and its Taylor polynomial of different degrees in the full inversion interval of $[0, \pi]$.

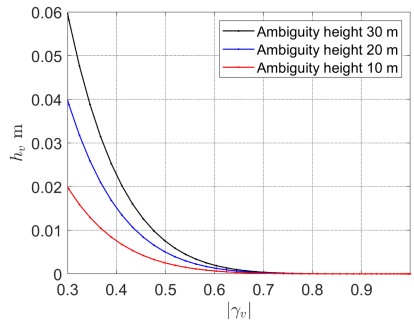

Fig. 4. Forest height approximation error of (12) with different ambiguity heights.

The series expansion of the inverse series of (8) is given by

$$x = a_0 + a_1 y + a_2 y^2 + \cdots. \tag{9}$$

Inserting (9) into (8) and equating the coefficients then gives [33], [34]

$$x = \sqrt{6(1-y)} + \frac{3}{10}\sqrt{\frac{3}{2}}(1-y)^{\frac{3}{2}} + \frac{321}{2800}\sqrt{\frac{3}{2}}(1-y)^{\frac{5}{2}} + \frac{3197}{56000}\sqrt{\frac{3}{2}}(1-y)^{\frac{7}{2}} + \frac{8151}{250880}\sqrt{\frac{3}{2}}(1-y)^{\frac{9}{2}} + o[1-y]^5. \tag{10}$$

Let $q = \sqrt{6(1-y)}$, we have

$$x = q + \frac{1}{40}q^3 + \frac{107}{67200}q^5 + \frac{3197}{24192000}q^7 + \frac{8151}{650280960}q^9 = q + \beta_1 q^3 + \beta_2 q^5 + \beta_3 q^7 + \beta_4 q^9. \tag{11}$$

Therefore, the forest height as a function of vertical wavenumber k_z and volume coherence γ_v is obtained as follows:

$$h_v = \frac{2}{k_z}\left(q + \beta_1 q^3 + \beta_2 q^5 + \beta_3 q^7 + \beta_4 q^9\right) \tag{12}$$

where $q = \sqrt{6(1-|\gamma_v|)}$.

Note that from (9) to (10), the higher-order terms are neglected. The approximation errors introduced by the higher-order terms are very small. Fig. 4 presents the approximation errors of (12). It indicates that the approximation errors of the model increase with the decrease in coherence. In practical inversion, a coherence less than 0.3 is considered to have a large potential error and is therefore masked out. As shown in Fig. 4, the approximation errors are less than 0.1 m, which has little

impact on the subsequent error analysis. In addition, the errors can be further reduced by considering higher-order terms.

Taking the derivative of (12) with respect to $|\gamma_v|$ yields

$$\frac{dh_v}{d\,|\gamma_v|} = -\frac{6}{k_z}\left(q^{-1} + 3\beta_1 q + 5\beta_2 q^3 + 7\beta_3 q^5 + 9\beta_4 q^7\right). \tag{13}$$

From (13), we have obtained the forest error transfer function concerning the perturbations of volume coherence

$$\Delta h_v = -\frac{6}{k_z}\left(q^{-1} + 3\beta_1 q + 5\beta_2 q^3 + 7\beta_3 q^5 + 9\beta_4 q^7\right)\Delta\,|\gamma_v| \tag{14}$$

where $q = \sqrt{6(1-|\gamma_v|)}$.

III. Error Model Derivation

This section examines the effects of channel imbalance, crosstalk, and noise on volume coherence. Then, the relationship between the nonideal system parameters and the forest height estimation error is established based on the error transfer function.

A. Problem Formulation

The effects of nonideal system parameters can be formulated as a two-stage linear process, and the measured scattering matrix $\mathbf{Z}$ is given by [35], [36], [37]

$$\begin{aligned}\mathbf{Z} &= \mathbf{R}_s \cdot \mathbf{S} \cdot \mathbf{T}_s + \mathbf{N}_s \\ &= \begin{bmatrix} 1 & \delta_h \\ \delta_v & f \end{bmatrix}\begin{bmatrix} S_{hh} & S_{hv} \\ S_{vh} & S_{vv} \end{bmatrix}\begin{bmatrix} 1 & \delta_v \\ \delta_h & f \end{bmatrix} + \begin{bmatrix} n_{hh} & n_{hv} \\ n_{vh} & n_{vv} \end{bmatrix}\end{aligned} \tag{15}$$

where $\mathbf{S}$ is the ideal scattering matrix, $\mathbf{R}_s$ and $\mathbf{T}_s$ denote the receiving and transmitting system, respectively, and $\mathbf{N}_s$ is the noise term. δ_h denotes the crosstalk when horizontally polarized electric fields are transmitted or received, δ_v denotes the crosstalk when vertically polarized electric fields are transmitted or received, and f represents the copolarized channel imbalance in amplitude and phase [35].

With the linear model in (15), it can be easily shown that the observed Pauli scattering vector is modified as

$$\begin{aligned}\vec{\mathbf{k}}_z &= \frac{1}{\sqrt{2}}\begin{bmatrix} \frac{1+\delta_v^2+\delta_h^2+f^2}{2} & \frac{1+\delta_v^2-\delta_h^2-f^2}{2} & \delta_h+\delta_v f \\ \frac{1-\delta_v^2+\delta_h^2-f^2}{2} & \frac{1-\delta_v^2-\delta_h^2+f^2}{2} & \delta_h-\delta_v f \\ \delta_v+\delta_h f & \delta_v-\delta_h f & \delta_v\delta_h+f \end{bmatrix} \\ &\quad\times\begin{bmatrix} S_{hh}+S_{vv} \\ S_{hh}-S_{vv} \\ 2S_{hv} \end{bmatrix} + \frac{1}{\sqrt{2}}\begin{bmatrix} n_{hh}+n_{vv} \\ n_{hh}-n_{vv} \\ 2n_{hv} \end{bmatrix} \\ &= \mathbf{Q}(\delta_h,\delta_v,f)\vec{\mathbf{k}}_s + \vec{\mathbf{n}}.\end{aligned} \tag{16}$$

The distortion matrix $\mathbf{Q}$ illustrates how the channel imbalance and crosstalk couple together and impact the Pauli scattering vector. The Pauli scattering vectors of two registered images with a spatial or temporal baseline can be described, using (16), as

$$\begin{aligned}\vec{\mathbf{k}}_{z,1} &= \mathbf{Q}\left(\delta_h,\delta_v,f\right)\vec{\mathbf{k}}_{s,1} + \vec{\mathbf{n}}_1 \\ \vec{\mathbf{k}}_{z,2} &= \mathbf{Q}\left(\delta_h,\delta_v,f\right)\vec{\mathbf{k}}_{s,2} + \vec{\mathbf{n}}_2.\end{aligned} \tag{17}$$

Assuming the system parameters are time-invariant, the two acquisitions $\vec{\mathbf{k}}_{z,1}$ and $\vec{\mathbf{k}}_{z,2}$ share the same distortion matrix. Assuming the noise and signal are uncorrelated [35], the polarimetric coherency matrices and polarimetric interferometry matrix can be obtained by the ensemble average [11] of the Pauli scattering vectors as

$$\begin{aligned}\mathbf{T}_1\left(\mathbf{Q},\vec{\mathbf{n}}_1\right) &= \left\langle \vec{\mathbf{k}}_{z,1}\cdot\vec{\mathbf{k}}_{z,1}^H \right\rangle = \mathbf{Q}\mathbf{T}_1\mathbf{Q}^H + \mathbf{N}_1 \\ \mathbf{T}_2\left(\mathbf{Q},\vec{\mathbf{n}}_2\right) &= \left\langle \vec{\mathbf{k}}_{z,2}\cdot\vec{\mathbf{k}}_{z,2}^H \right\rangle = \mathbf{Q}\mathbf{T}_2\mathbf{Q}^H + \mathbf{N}_2 \\ \mathbf{\Omega}\left(\mathbf{Q}\right) &= \left\langle \vec{\mathbf{k}}_{z,1}\cdot\vec{\mathbf{k}}_{z,2}^H \right\rangle = \mathbf{Q}\mathbf{\Omega}\mathbf{Q}^H\end{aligned} \tag{18}$$

where $\mathbf{N}_i$ is the covariance matrix of the noise. The ideal coherence and polarimetric interferometry matrix is given by [11]

$$\mathbf{T}_i = \left\langle \vec{\mathbf{k}}_{s,i}\cdot\vec{\mathbf{k}}_{s,i}^H \right\rangle, \mathbf{\Omega} = \left\langle \vec{\mathbf{k}}_{s,1}\cdot\vec{\mathbf{k}}_{s,2}^H \right\rangle. \tag{19}$$

B. Impact on Volume Coherence

We now turn to consider the impact of these nonideal system parameters on volume coherence in more detail. The volume coherence is obtained through the phase diversity method [12], which needs to solve the following eigendecomposition problem

$$\left[-j(\mathbf{\Omega}-\mathbf{\Omega}^H)\right]^{-1}\left(\mathbf{\Omega}+\mathbf{\Omega}^H\right)\vec{\mathbf{w}} = \lambda\vec{\mathbf{w}}. \tag{20}$$

The optimum coherences with the largest and smallest ground-to-volume scattering ratio can be obtained according to the definition of complex interferometric coherence

$$\gamma(\vec{\mathbf{w}}) = \frac{\vec{\mathbf{w}}^H\mathbf{\Omega}\vec{\mathbf{w}}}{\vec{\mathbf{w}}^H\mathbf{T}\vec{\mathbf{w}}} \tag{21}$$

where $\vec{\mathbf{w}}$ denotes the eigenvectors corresponding to the largest and smallest eigenvalue, and $\mathbf{T} = \frac{1}{2}(\mathbf{T}_1+\mathbf{T}_2)$ assuming reciprocity principle.

Substitution of the distorted polarimetric interferometry matrix in (18) to (20) yields

$$\begin{aligned}&\left[-j\left(\mathbf{Q}\mathbf{\Omega}\mathbf{Q}^H - \mathbf{Q}\mathbf{\Omega}^H\mathbf{Q}^H\right)\right]^{-1}\left(\mathbf{Q}\mathbf{\Omega}\mathbf{Q}^H + \mathbf{Q}\mathbf{\Omega}^H\mathbf{Q}^H\right) \\ &= \left(\mathbf{Q}^H\right)^{-1}\left[-j\left(\mathbf{\Omega}-\mathbf{\Omega}^H\right)\right]^{-1}\mathbf{Q}^{-1}\mathbf{Q}\left(\mathbf{\Omega}+\mathbf{\Omega}^H\right)\mathbf{Q}^H \\ &= \left(\mathbf{Q}^H\right)^{-1}\left[-j\left(\mathbf{\Omega}-\mathbf{\Omega}^H\right)\right]^{-1}\left(\mathbf{\Omega}+\mathbf{\Omega}^H\right)\mathbf{Q}^H.\end{aligned} \tag{22}$$

The above matrix is a similarity transformation of the matrix in (20). It means they share the same eigenvalues, and there is a linear transformation relationship between their eigenvectors. Specifically, if $\vec{\mathbf{w}}$ is an eigenvector of (20), $\mathbf{Q}^{-H}\vec{\mathbf{w}}$ is an eigenvector of (22). Suppose $\vec{\mathbf{w}}_v$ is the eigenvector of (20), and it corresponds to the volume coherence. Then, $\mathbf{Q}^{-H}\vec{\mathbf{w}}_v$ is an eigenvector of (22). Substitution of $\mathbf{Q}^{-H}\vec{\mathbf{w}}_v$ and (18) in (21) gives the distorted volume coherence

$$\begin{aligned}\tilde{\gamma}_1 &= \frac{\left(\mathbf{Q}^{-H}\vec{\mathbf{w}}_v\right)^H\mathbf{Q}\mathbf{\Omega}\mathbf{Q}^H\left(\mathbf{Q}^{-H}\vec{\mathbf{w}}_v\right)}{\left(\mathbf{Q}^{-H}\vec{\mathbf{w}}_v\right)^H\left(\mathbf{Q}\mathbf{T}\mathbf{Q}^H+\mathbf{N}\right)\left(\mathbf{Q}^{-H}\vec{\mathbf{w}}_v\right)} \\ &= \frac{\vec{\mathbf{w}}_v^H\mathbf{\Omega}\vec{\mathbf{w}}_v}{\vec{\mathbf{w}}_v^H\left(\mathbf{T}+\mathbf{Q}^{-1}\mathbf{N}\mathbf{Q}^{-H}\right)\vec{\mathbf{w}}_v} \\ &= \frac{\gamma_1}{1+\frac{\vec{\mathbf{w}}_v^H\mathbf{Q}^{-1}\mathbf{N}\mathbf{Q}^{-H}\vec{\mathbf{w}}_v}{\vec{\mathbf{w}}_v^H\mathbf{T}\vec{\mathbf{w}}_v}}\end{aligned} \tag{23}$$

where $\mathbf{N} = (\mathbf{N}_1+\mathbf{N}_2)/2$ and γ_1 is the estimated volume coherence without any distortion. To further explore the impact of

crosstalk, channel imbalance, and noise on volume coherence, we concentrate on the term in the denominator of (23).

First, we define the noise-signal ratio (NSR) at a given polarization channel $\vec{\mathbf{w}}_v$ as [38]

$$\mathrm{NSR}(\vec{\mathbf{w}}_v) = \frac{\vec{\mathbf{w}}_v^H \mathbf{N} \vec{\mathbf{w}}_v}{\vec{\mathbf{w}}_v^H \mathbf{T} \vec{\mathbf{w}}_v}. \tag{24}$$

After comparing (24) and (23), we conclude that the crosstalk and channel imbalance influence the volume coherence through the distortion matrix $\mathbf{Q}$ by modifying $\mathrm{NSR}(\vec{\mathbf{w}}_v)$. Concretely, the modified $\tilde{\mathrm{NSR}}(\vec{\mathbf{w}}_v)$ has the form of

$$\tilde{\mathrm{NSR}}(\vec{\mathbf{w}}_v) = \frac{(\mathbf{Q}^{-H}\vec{\mathbf{w}}_v)^H \mathbf{N} (\mathbf{Q}^{-H}\vec{\mathbf{w}}_v)}{\vec{\mathbf{w}}_v^H \mathbf{T} \vec{\mathbf{w}}_v}. \tag{25}$$

The matrix $\mathbf{Q}$ can be decomposed as

$$\mathbf{Q} = \mathbf{U}\mathbf{\Lambda}\mathbf{U}^{-1}, \text{with } \mathbf{\Lambda} = \mathrm{diag}\left\{\lambda_i\right\}, \mathbf{U} = [\vec{\mathbf{u}}_1, \vec{\mathbf{u}}_2, \vec{\mathbf{u}}_3]. \tag{26}$$

As the eigenvalues of $\mathbf{Q}^H$ are the complex conjugates of the eigenvalues of $\mathbf{Q}$, $\mathbf{Q}^{-H}$ can be written as

$$\mathbf{Q}^{-H} = \mathbf{V}\mathbf{\Lambda}^{-H}\mathbf{V}^{-1}, \text{with } \mathbf{V} = [\vec{\mathbf{v}}_1, \vec{\mathbf{v}}_2, \vec{\mathbf{v}}_3]. \tag{27}$$

Under the eigenbasis of $\mathbf{Q}^{-H}$, $\vec{\mathbf{w}}_v$ can be expressed as

$$\vec{\mathbf{w}}_v = \alpha_1 \vec{\mathbf{v}}_1 + \alpha_2 \vec{\mathbf{v}}_2 + \alpha_3 \vec{\mathbf{v}}_3. \tag{28}$$

Typical channel imbalances are on the order of one, and crosstalks and noise levels are about -10 to -30 dB, respectively. Therefore, $\mathbf{Q}$ is always invertable. If $\delta_h = \delta_v = 0, f = 1$ then the system has zero crosstalk and channel imbalance. In this case, $\mathbf{Q}$ reduces to an identity matrix. Substitution of (28) in the numerator of (25) yields

$$\begin{aligned}
&(\mathbf{Q}^{-H}\vec{\mathbf{w}}_v)^H \mathbf{N} \mathbf{Q}^{-H} \vec{\mathbf{w}}_v \\
&= \left(\sum_i \alpha_i \mathbf{Q}^{-H} \vec{\mathbf{v}}_i\right)^H \mathbf{N} \left(\sum_i \alpha_i \mathbf{Q}^{-H} \vec{\mathbf{v}}_i\right) \\
&= \left(\sum_i \alpha_i{}^* (\lambda_i)^{-1} \vec{\mathbf{v}}_i{}^H\right) \mathbf{N} \left(\sum_i \alpha_i (\lambda_i{}^*)^{-1} \vec{\mathbf{v}}_i\right).
\end{aligned} \tag{29}$$

The above equation shows how the distortion matrix $\mathbf{Q}$ affects $\mathrm{NSR}(\vec{\mathbf{w}}_v)$, and the extent of this effect depends on $\vec{\mathbf{w}}_v$. For instance, if $\vec{\mathbf{w}}_v$ coincides with $\vec{\mathbf{v}}_i$, $\mathrm{NSR}(\vec{\mathbf{w}}_v)$ will be altered by a factor of $|\lambda_i|^{-2}$. Since that $\vec{\mathbf{w}}_v$ is typically a linear combination of the eigenvectors, the change of $\mathrm{NSR}(\vec{\mathbf{w}}_v)$ becomes a linear combination of the corresponding eigenpairs. Therefore, we define a migration factor A to quantify the distortion of $\mathrm{NSR}(\vec{\mathbf{w}}_v)$ introduced by $\mathbf{Q}$

$$\tilde{\mathrm{NSR}}(\vec{\mathbf{w}}_v) = A \cdot \mathrm{NSR}(\vec{\mathbf{w}}_v). \tag{30}$$

From (24), (25), and (30), it is evident that (23) can be reexpressed as

$$\tilde{\gamma}_1 = \frac{\gamma_1}{1 + A \cdot \mathrm{NSR}(\vec{\mathbf{w}}_v)}. \tag{31}$$

With (31), $\Delta|\gamma_v|$ is given by

$$\Delta\,|\gamma_v| = |\tilde{\gamma_1}| - |\gamma_1| = -A \cdot \mathrm{NSR}(\vec{\mathbf{w}}_v)|\tilde{\gamma_1}|. \tag{32}$$

Then, substitution of (32) in (14) yields the forest height estimation error model

$$\begin{aligned}
&\Delta h_v(|\tilde{\gamma_1}|, \mathrm{SNR}, \delta_h, \delta_v, f, k_z) \\
&= \frac{6}{k_z}\left(q^{-1} + 3\beta_1 q + 5\beta_2 q^3 + 7\beta_3 q^5 + 9\beta_4 q^7\right) \\
&\cdot |\tilde{\gamma_1}| \cdot A \cdot \mathrm{NSR}(\vec{\mathbf{w}}_v)
\end{aligned} \tag{33}$$

with $q = \sqrt{6(1 - |\gamma_1|)}$ and the coefficients β_i can be found in (11).

In the error model of (33), A and $\mathrm{NSR}(\vec{\mathbf{w}}_v)$ should be considered in more detail. Generally, A and $\mathrm{NSR}(\vec{\mathbf{w}}_v)$ cannot be explicitly derived as they are related to the eigenvector of the uncontaminated data and noise as shown in (24) and (29). However, they could be considered from a statistical point of view. The migration factor A can be defined as the average impact of each eigenvalue

$$A = \frac{1}{3}\sum_i |\lambda_i|^{-2} \tag{34}$$

and the three eigenvalues of $\mathbf{Q}$ can be explicitly derived as

$$\begin{aligned}
\lambda_1 &= \frac{1}{2}\left(-\sqrt{(f+1)^2(4\delta_h\delta_v + (f-1)^2)} + 2\delta_h\delta_v + f^2 + 1\right) \\
\lambda_2 &= \frac{1}{2}\left(\sqrt{(f+1)^2(4\delta_h\delta_v + (f-1)^2)} + 2\delta_h\delta_v + f^2 + 1\right) \\
\lambda_3 &= f - \delta_h\delta_v.
\end{aligned} \tag{35}$$

The inverse of the SNR of the system is a good approximation of $\mathrm{NSR}(\vec{\mathbf{w}}_v)$

$$\frac{1}{\mathrm{SNR}} \simeq \mathrm{NSR}(\vec{\mathbf{w}}_v). \tag{36}$$

Then, substitution of (34)–(36) in (33) will give the final forest height estimation error model.

C. Analysis of the Forest Height Error Model

As shown in (34) and (35), δ_h and δ_v play the same role in the migration factor. It suggests that both HV and VH crosstalks deserve equal consideration when designing the system parameters. Without loss of generality, the crosstalk is assumed to be characterized by $\delta_h = \delta_v = \delta$ in the following text unless otherwise specified.

The channel imbalance f influences $\mathrm{NSR}(\vec{\mathbf{w}}_v)$ on twofolds, including amplitude imbalance $|f|$ and phase imbalance $\arg(f)$. The phase imbalance $\arg(f)$ should be considered from two aspects. Assuming there are no vertical and horizontal crosstalks. In this case, the eigenvalues in (35) degenerate as

$$\lambda_1 = 1, \quad \lambda_2 = f^2, \quad \lambda_3 = f. \tag{37}$$

Thus, the migration factor A in (34) is given by

$$A = \frac{1}{3}\left(1 + \frac{1}{|f|^2} + \frac{1}{|f|^4}\right). \tag{38}$$

Therefore, the phase imbalance $\arg(f)$ does not affect the inversion at all under this special case. In general, the migration factor is written as the form of the amplitude of eigenvalues when there

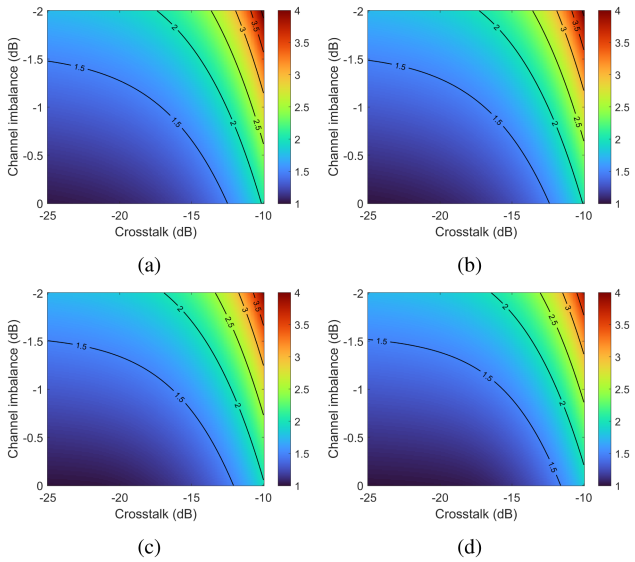

Fig. 5. Contour map of the migration factor as a function of channel imbalance and crosstalk with different phase imbalances. (a) Phase imbalances of 0°. (b) Phase imbalances of 5°. (c) Phase imbalances of 10°. (d) Phase imbalances of 15°.

are vertical and horizontal crosstalks. Therefore, the impact of phase imbalance $\arg(f)$ will be effectively counteracted. This conclusion will be validated through experiments in Section IV.

Fig. 5 presents the contour maps of the migration factor as a function of channel imbalance and crosstalk with different phase imbalances. As the figure shows, when the system parameters approach the ideal values, the migration factor closely approximates 1. In this case, the impact of channel imbalance and crosstalk on the system is minimal. However, the migration factor increases with the deterioration of crosstalk or channel imbalance. It implies that the system noise will be amplified once channel imbalance and crosstalk are unreasonably designed. In addition, the impact of channel phase imbalance is minimal as the migration factor is not sensitive to its variation.

Another special case is that system noise is very small, i.e., $\mathrm{NSR}(\vec{\mathbf{w}}_v) \to 0$, and the volume coherence remains invariant [27] to the calibration errors as shown in (31). In the following, it is shown that not only the optimized volume coherence but also the shape of the coherence region is not affected by the crosstalk and channel imbalance. In this case, the covariance matrices of the noise in (18) are null matrices. According to (21), the coherence is given by

$$\tilde{\gamma}(\vec{\mathbf{w}}) = \frac{\vec{\mathbf{w}}^H \left(\mathbf{Q}\mathbf{\Omega}\mathbf{Q}^H\right) \vec{\mathbf{w}}}{\vec{\mathbf{w}}^H \left(\mathbf{Q}\mathbf{T}\mathbf{Q}^H\right) \vec{\mathbf{w}}} = \frac{\left(\mathbf{Q}^H\vec{\mathbf{w}}\right)^H \mathbf{\Omega} \left(\mathbf{Q}^H\vec{\mathbf{w}}\right)}{\left(\mathbf{Q}^H\vec{\mathbf{w}}\right)^H \mathbf{T} \left(\mathbf{Q}^H\vec{\mathbf{w}}\right)}. \tag{39}$$

Obviously, the distortion matrix $\mathbf{Q}$ influences the phase and amplitude of the coherence. Concretely, the coherence changes as follows:

$$\gamma(\vec{\mathbf{w}}) \to \gamma(\mathbf{Q}^H\vec{\mathbf{w}}). \tag{40}$$

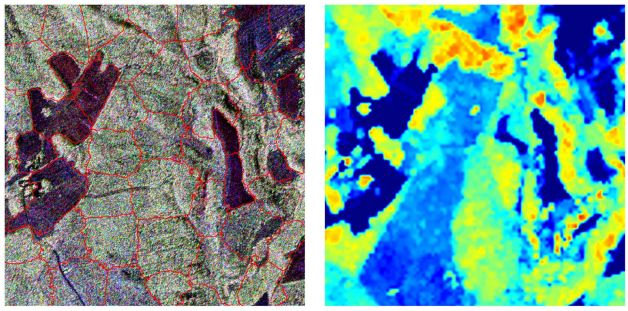

(a) (b)

Fig. 6. (a) Pauli-basis color composite map. (b) LiDAR H100 height map. The polygons are used in the forest height validation, and the color ramp ranges from 0 (blue) to 30 m (red).

TABLE I
POLINSAR DATA PARAMETERS

Master	Slave	Baseline (m)	k_z range	ID
Bio0202	Bio0206	6	0.073-0.162	BL1
Bio0202	Bio0208	12	0.155-0.282	BL2
Bio0202	Bio0210	18	0.194-0.391	BL3

As a result, the coherence originally observed in the polarization channel $\vec{\mathbf{w}}$ is transformed into a different polarization channel $\mathbf{Q}^H\vec{\mathbf{w}}$ due to the distortion matrix $\mathbf{Q}$. However, the coherence region is not changed. In this particular case, the forest height will not be affected by the crosstalk and channel imbalance as long as the inversion method uses the coherence-region-based optimized coherence in the inversion stage.

IV. EXPERIMENTAL RESULTS

A. Data

The test site, Krycklan river catchment (KCS) is located in the boreal region of northern Sweden in Västerbotten County. The KCS comprises a mosaic of instrumented and well-studied forests, agriculture, wetlands, and lakes, all drained and connected by a network of streams and rivers [39]. Mixed coniferous forest is the dominant forest type in the experimental area, primarily between 0 and 30 m in height [26].

The datasets used for this study were acquired by the German Aerospace Center (DLR) E-SAR system. The BioSAR campaign was carried out in October 2008 in the KCS [40]. Fig. 6(a) shows the Pauli-basis polarimetric composite image, and Fig. 6(b) provides the LiDAR H100 forest height map.

To comprehensively verify the error model in (33), three repeat-pass PolInSAR pairs with baseline lengths of 6, 12, and 18 are used in this study, and the corresponding parameters are listed in Table. I. Fig. 7 presents the histogram of the vertical wavenumber of three baselines. The significant variations among different baselines will facilitate the validation of the effect of the vertical wavenumber.

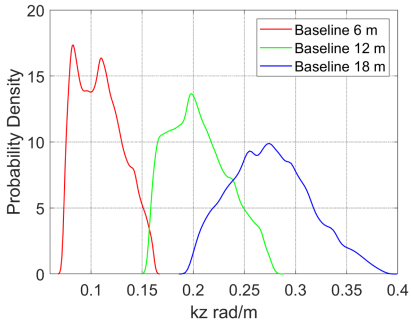

Fig. 7. Histogram of the vertical wavenumber in different baselines.

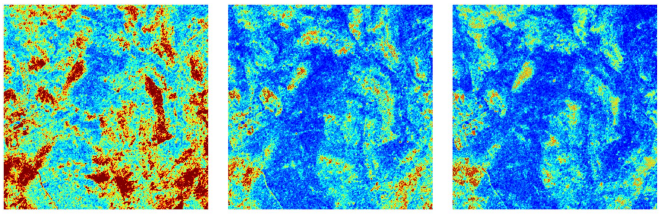

Fig. 8. Inversion results from different baselines, and the color ramp ranges from 0 (blue) to 30 m (red). (a) BL1. (b) BL2. (c) BL3.

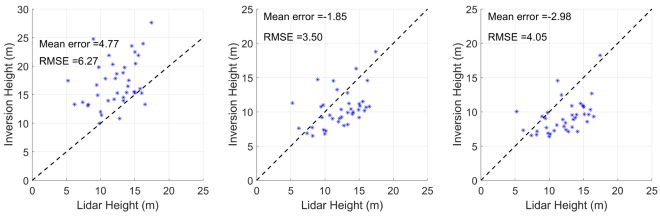

Fig. 9. Correlation plots between inversion results and LiDAR heights. (a) BL1. (b) BL2. (c) BL3.

B. Inversion Results

Following the inversion scheme in Section II, the PolInSAR forest height maps from different baselines are shown in Fig. 8. There is a considerable variation in the inverted forest heights across different baselines. Specifically, the inverted forest heights decrease significantly with increasing the spatial baseline. The short baseline BL1 exhibits a severe overestimation, while the long baseline BL3 shows a slight underestimation. In contrast, the moderate spatial baseline BL2 presents relatively more accurate and robust results.

In Fig. 9, the correlation plots and quantitative evaluations with the polygons are plotted against the LiDAR H100 height. The scatter points of BL1 and BL3 deviate from the ideal straight line, indicating an overestimation and underestimation, respectively. BL2 shows the best results with a mean error of -1.85 m and RMSE of 3.50 m, and it successfully reduces the overestimation and underestimation in BL1 and BL3, respectively. Subsequent experiments are conducted mainly using BL2, while BL1 and BL3 are used to verify the effect of vertical wavenumber.

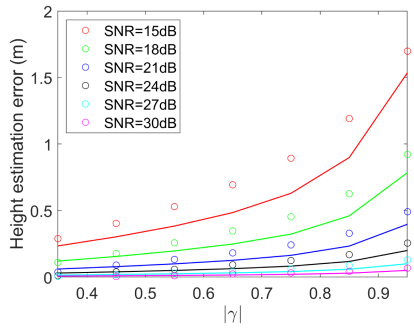

Fig. 10. Observed and theoretical errors as a function of the volume coherence with different SNRs. The solid lines indicate the predicted errors of (33), while the dots indicate the observed errors.

C. Error Simulation

Based on the PolInSAR measurements with different baselines, the performance of the error models is experimentally validated, including the proposed model and a published model LPA (see the Appendix) [28].

To validate the error model, we artificially added various polarimetric system parameters to the original SAR data. In the following text, the corresponding uncontaminated heights denote the estimated forest heights using the original SAR data. The forest height errors refer to the variation of the inverted forest height compared with the uncontaminated heights with the deterioration of system parameters. As shown in (33), the forest height error model is a multivariate function in terms of six physical parameters: channel imbalance f, crosstalk δ_h, δ_v, SNR, volume coherence γ_v and vertical wavenumber k_z. Five sets of comparative experiments are implemented to facilitate further analysis of the error model. Concretely, the first experiment concerns the noise-only system. The second set of experiments concerns the symmetrical effect of δ_h, δ_v. Then, the third experiment considers the coupled impacts of crosstalks and channel imbalance. The fourth experiment tends to validate the impacts of channel phase imbalance. Finally, the influence of vertical wavenumber is presented in the last experiment.

For the noise-only system $\Delta h_v(|\tilde{\gamma}_1|, \mathrm{SNR}, 0, 0, 1, k_z)$, only the complex Gaussian noise is added to the original SAR data. Seven volume coherence intervals are linearly divided from [0.3,1]. Coherence lower than 0.3 often generates unstable inversion and thus has been excluded. To reduce the influence of random noise and present the underlying relationship, the observed and theoretical errors are averaged calculated, and plotted at the middle point for each interval. Fig. 10 shows the observed and theoretical errors of (33) as a function of the volume coherence with different SNRs. Obviously, the forest height estimation errors increase with the deterioration of SNR and the increasing in the amplitude of volume coherence. Although the theoretical errors are slightly underestimated compared with the observed errors at low SNR, the curves fit the circles very well and show the same trend.

After analysis of the noise-only system, the symmetrical effects of HV and VH crosstalks are explored. In comparative experiments, the HV and VH crosstalks are varied in three pairs

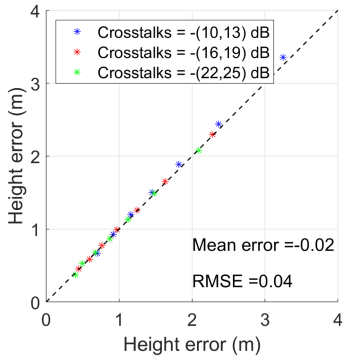

Fig. 11. Comparison plot between the observed errors. The horizontal axis represents the observation error with $\delta_h = \delta_1, \delta_v = \delta_2$, while the vertical axis represents the observation error when the values of δ_h and δ_v are interchanged, namely, $\delta_h = \delta_2, \delta_v = \delta_1$ under the same experimental conditions.

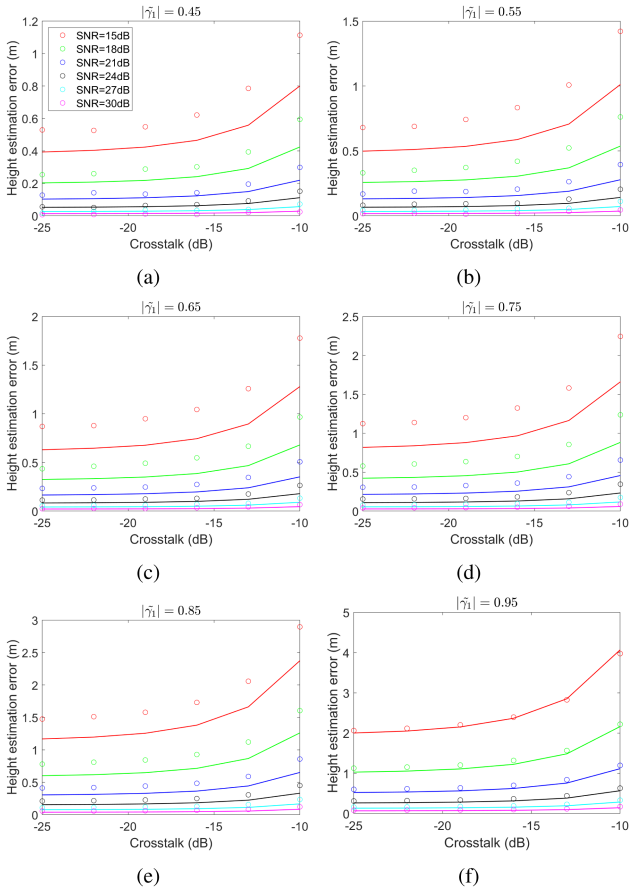

Fig. 12. Observed and theoretical errors as a function of the crosstalk with a fixed channel imbalance $f = -1$ dB.

of parameters, respectively. Fig. 11 shows the observed errors of (33) as a function of crosstalks δ_h and δ_v with a fixed channel imbalance $f = -1$ dB, and SNR $= 15$ dB. The small mean error and RMSE indicate that the HV and VH crosstalks play the same role in the forest height error model.

Then, the coupled effects of channel imbalance and crosstalk are presented. Note that the phase imbalance is not considered, and its influence is verified later. Fig. 12 shows the observed and theoretical errors of (33) as a function of crosstalk δ with a

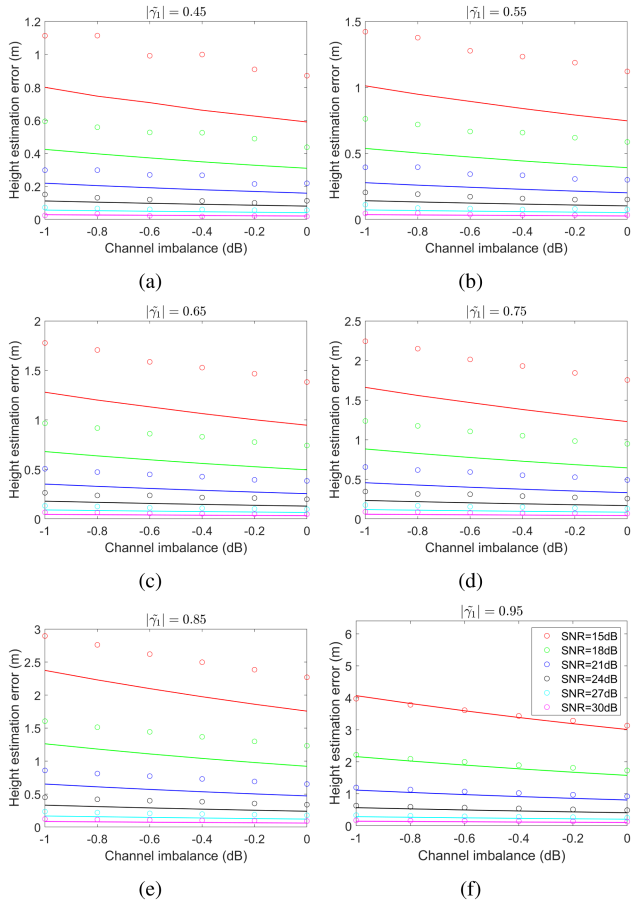

Fig. 13. Observed and theoretical errors as a function of the channel imbalance with fixed crosstalk $\delta = -10$ dB.

fixed channel imbalance $f = -1$ dB. Fig. 13 presents the observed and theoretical errors of (33) as a function of channel imbalance f with a fixed crosstalk $\delta = -10$ dB. As shown in Figs. 12 and 13, the forest height estimation errors increase with the deterioration of channel imbalance f and crosstalk δ. It is consistent with the trend of migration factor as shown in Fig. 5. In addition, the overall match between the curves and the circles suggests a good fit between the underlying theoretical model and the observed error. Interestingly, the model shows a better performance at larger volume coherence, as shown in Figs. 12(f) and 13(f). This surprising result can be due to the polynomial model in (33). At large $|\tilde{\gamma}_1|$, the perturbation of the noise is relatively small, and thus the model matches the observations better.

Then, the comparisons between the theoretical and observed errors are shown in Fig. 14. A strong correlation between theoretical and observed errors is observed. Consistent with the previous analysis, the slight negative mean errors indicate an underestimation of the theoretical error. Moreover, the small RMSE reveals a good match between the theoretical model and the observed errors. This implies that the theoretical model accurately captures the underlying patterns and trends present in the observed data, leading to minimal discrepancies between the predicted and actual errors.

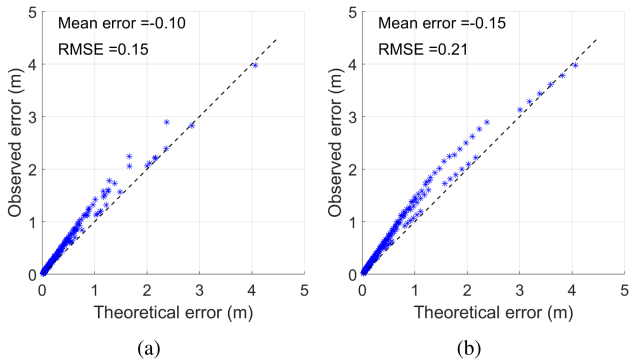

Fig. 14. Theoretical errors versus the observed errors. (a) With different crosstalk and SNRs as shown in Fig. 12. (b) With different channel imbalance and SNRs as shown in Fig. 13.

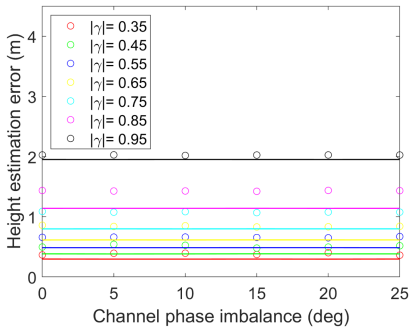

Fig. 15. Observed and theoretical errors as a function of the channel phase imbalance with $f = -1$ dB, $\delta = 0$ and SNR $= -15$ dB.

In addition, Section III concludes that the forest heights estimation errors are not sensitive to the channel phase imbalance. Fig. 15 presents the forest height estimation errors as a function of channel phase imbalance with $f = -1$ dB, $\delta = 0$ and SNR $= -15$ dB. As the figure shows, the theoretical and observed errors hardly change with the increase of the channel phase imbalance. It demonstrates that the phase imbalance is not amplifying the forest height estimation.

As the crosstalks and the channel imbalance are coupled with each other, the effect of phase imbalance should also be considered with crosstalks. Fig. 16 shows the observed and theoretical errors as a function of the channel phase imbalance and crosstalk with SNR $= 15$ dB and $f = -1$ dB. As the results show, the forest height estimation errors are not sensitive to channel phase imbalance, even in the presence of polarization crosstalk. Moreover, the sensitivity becomes smaller as system parameters improve. Interestingly, as the phase imbalance increases, the forest height estimation errors have a slightly decreasing trend. This is due to the fact that the migration factor becomes smaller as the phase imbalance increases. This phenomenon is also verified by the offset of the contours of the migration factor with the increase of phase as shown in Fig. 5.

Finally, the effect of vertical wavenumber is analyzed by three baselines, and Fig. 17 shows the forest height estimation errors. The height errors of different baselines vary significantly. As the model (33) predicts, the shorter baseline suffers the larger height

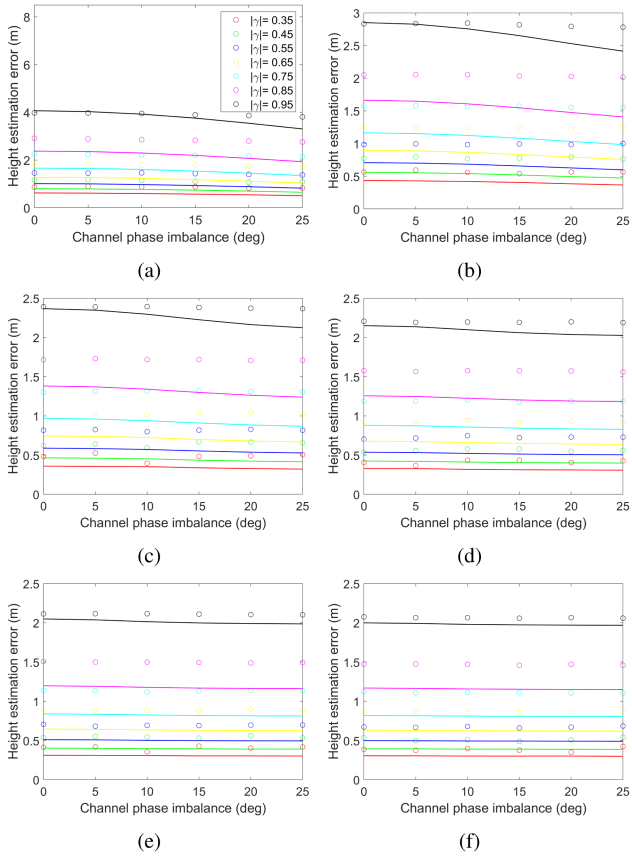

Fig. 16. Observed and theoretical errors as a function of the channel phase imbalance and crosstalk with SNR $= 15$ dB and $f = -1$ dB. (a) $\delta = -10$ dB. (b) $\delta = -13$ dB. (c) $\delta = -16$ dB. (d) $\delta = -19$ dB. (e) $\delta = -22$ dB. (f) $\delta = -25$ dB.

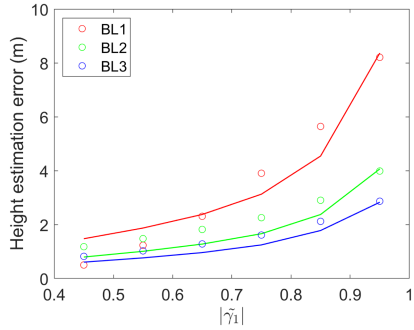

Fig. 17. Observed and theoretical errors in different baselines. Note that the system parameters are as SNR $= 15$ dB, $\delta = -10$ dB, and $f = -1$ dB.

error since it is more sensitive to the variation of $|\tilde{\gamma}_1|$ than the other baseline.

D. Comparison With Other Error Model

The results of LPA are presented in Figs. 18 and 19. As the figures show, the theoretical errors by (42) are overestimated at high SNR and underestimated at low SNR. In addition, the overestimation is particularly severe at high coherence, while the underestimation is more serious at low coherence. For example, the model prediction errors are even nearly twice the observation errors as the red curves and dots shown in Figs. 18(e) and (f),

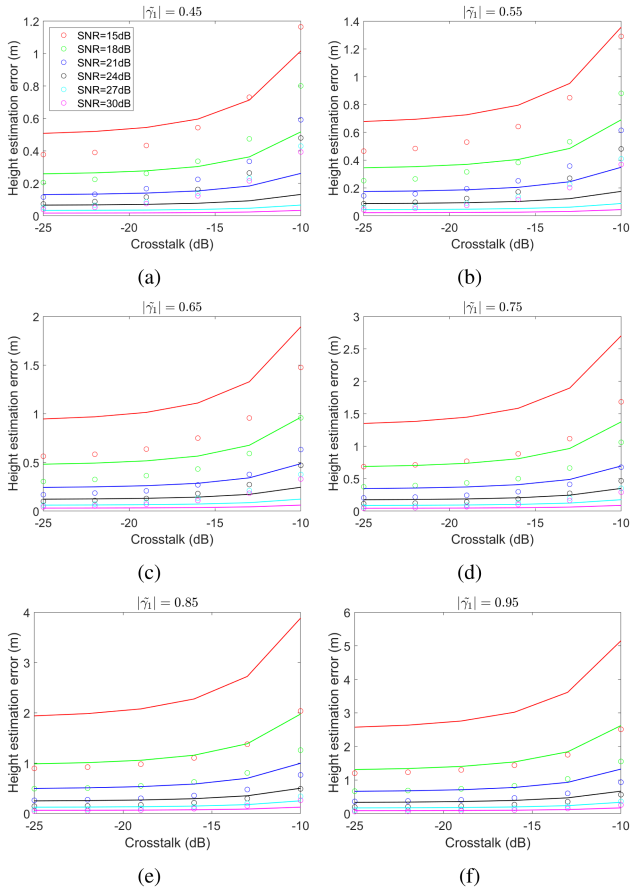

Fig. 18. Observed and theoretical errors as a function of the crosstalk and SNR with a fixed channel imbalance $f = -1$ dB. (a) $|\tilde{\gamma}_1| = 0.45$. (b) $|\tilde{\gamma}_1| = 0.55$. (c) $|\tilde{\gamma}_1| = 0.65$. (d) $|\tilde{\gamma}_1| = 0.75$. (e) $|\tilde{\gamma}_1| = 0.85$. (f) $|\tilde{\gamma}_1| = 0.95$.

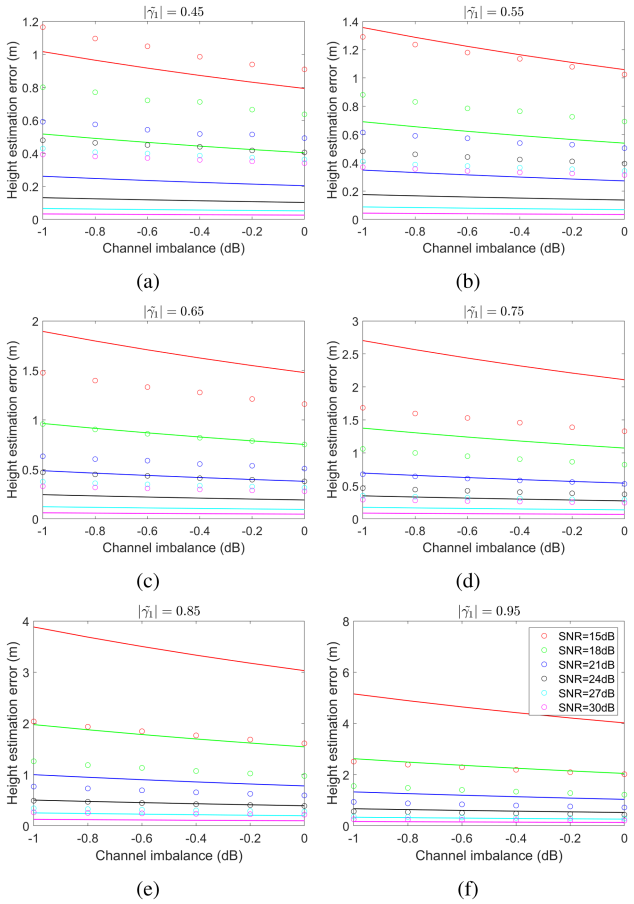

Fig. 19. Observed and theoretical errors as a function of the channel imbalance and SNR with fixed crosstalk $\delta = -10$ dB. (a) $|\tilde{\gamma}_1| = 0.45$. (b) $|\tilde{\gamma}_1| = 0.55$. (c) $|\tilde{\gamma}_1| = 0.65$. (d) $|\tilde{\gamma}_1| = 0.75$. (e) $|\tilde{\gamma}_1| = 0.85$. (f) $|\tilde{\gamma}_1| = 0.95$.

and 19(e) and (f). However, the model prediction errors are much smaller than the observation errors as the red curves and dots shown in Figs. 18(a) and (b), and 19(a) and (b).

Fig. 20 shows the comparisons between the theoretical and the observed errors. A strong variation of the theoretical errors is found evident for LPA, which may be attributed to neglecting the influence of the first term in (41). To compensate its influence, the model introduces an empirical parameter C, which is determined by least-square [28].

Therefore, the least squares fitting on C is performed to explore its influence [28]. The complex Gaussian noise with different SNRs is added with $\delta = 0, f = 1$. The optimal empirical parameter C is found to be 1.65. As shown in Fig. 21, the comparisons between the theoretical and the observed errors have been greatly improved after recalculating the empirical parameter. Therefore, the performance of LPA strongly depends on the empirical parameter, which is varied with the used datasets. It reduces the generalization performance of the model.

Overall, these experiments provide strong evidence for the effectiveness of the proposed model in capturing and explaining the effects of polarimetric system parameters on the forest height estimation error. In addition, the proposed error model can achieve a more robust and accurate prediction of the forest height estimation error than the LPA model.

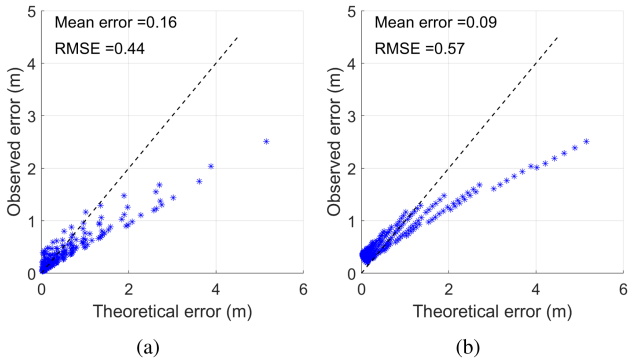

Fig. 20. Theoretical errors versus the observed errors. (a) With different crosstalks and SNRs as shown in Fig. 18. (b) With different channel imbalances and SNRs as shown in Fig. 19.

V. Discussion

The main purpose of establishing the forest height error model is to facilitate the PolInSAR system parameters designing and systematic error correction. The proposed forest height error model has been validated through comprehensive experiments in Section IV. Subsequently, we will discuss how to apply it in the PolInSAR system parameters designing, the error correction, and the limitations.

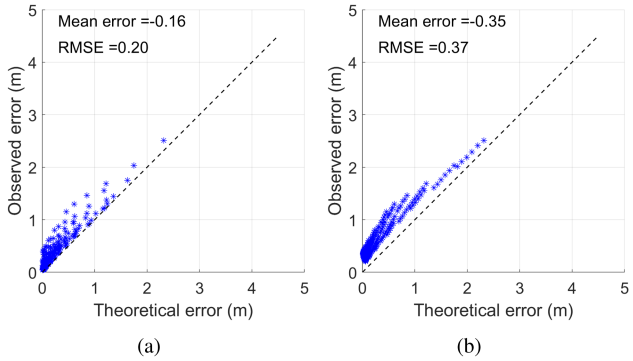

Fig. 21. Theoretical errors versus the observed errors after recalculating the empirical parameter. (a) With different crosstalks and SNRs. (b) With different channel imbalances and SNRs.

A. System Parameters Designing

As shown in (33), the forest height error model is a multivariate function in terms of six physical parameters: the volume coherence γ_v, vertical wavenumber k_z, channel imbalance f, crosstalk δ_h, δ_v, and SNR. Between these parameters, vertical wavenumber k_z, channel imbalance f, crosstalk δ_h, δ_v, and SNR are known as the system parameters while the volume coherence γ_v denotes the model parameter. Therefore, the system parameter designing is to analyze and optimize k_z, f, δ_h, δ_v, and SNR under the interplay of γ_v.

To design the PolInSAR system, one can determine the vertical wavenumber and select the other polarimetric system parameters by retrieving the look-up table of the error map. For example, it is required to design the PolInSAR system parameters for a specific scene. In this experimental area, the forest heights are generally less than 30 m. The objective is to ensure that the height errors resulting from the system parameters should be less than 0.7 m. First, the vertical wavenumber should be larger than 0.08 rad/m [41]. With the vertical wavenumber, the look-up table of height estimation error can be obtained according to the error model in (33). Fig. 22 presents the contour maps of height estimation errors as a function of channel imbalance, crosstalk, and coherence with different SNRs with a fixed $|\tilde{\gamma}_1| = 0.7$. Since the error model (33) is an increasing function with respect to the coherence amplitude, a coherence amplitude of 0.7 will cover most cases. According to Fig. 22, in order to satisfy the system requirements, one possible strategy may be SNR > 20 dB, $\delta < -15$ dB, and $f > -0.7$ dB. In addition, the phase imbalance will still affect the phase accuracy of the coherence, so the parameter should be as small as possible. It is worth noting that the viable option is not the only one. The system designer can determine a feasible solution based on a compromise between various parameters.

B. Forest Height Correction

The forest height estimation error can be divided into two components: the model error and the systematic error. Model error is the estimation error due to the inaccuracy of the forest height model, and systematic errors are caused by imperfect system parameters. The error model can not only provide a reference for system parameter design but also be used for forest height systematic error correction.

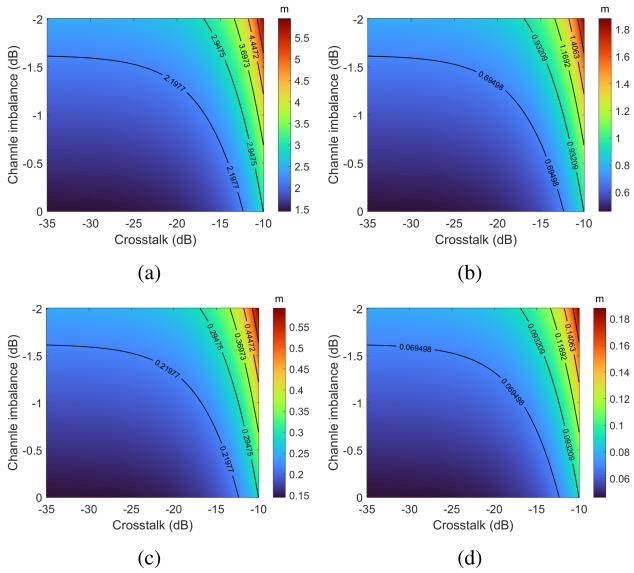

Fig. 22. Look-up table of height estimation error as a function of channel imbalance, crosstalk, and coherence with different SNRs. All the simulation maps share the same vertical wavenumber of 0.08 rad/m. (a) SNR = 15 dB. (b) SNR = 20 dB. (c) SNR = 25 dB. (d) SNR = 30 dB.

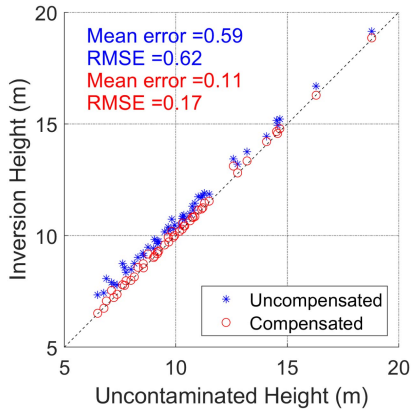

Fig. 23. Correlation plots between inversion results and uncontaminated heights.

Assume that the system parameters are SNR $= 20$ dB, $\delta = -15$ dB, and $f = -0.7$ dB. Then, one can compensate for the estimation errors according to (33). Fig. 23 shows the comparison plot between the estimated heights and the uncontaminated heights. The mean error between the estimated and uncontaminated height is 0.59 m with an RMSE of 0.62 m before compensation. It indicates that the designed system parameters meet the requirements. After compensation, the mean error and RMSE become 0.11 m and 0.17 m, respectively. It demonstrates that the error model (33) can effectively reduce the forest height systematic error and achieve a good forest height error correction.

C. Model Applicability Analysis and Limitations

The experimental results demonstrate that the model can accurately capture the impacts of nonideal system parameters

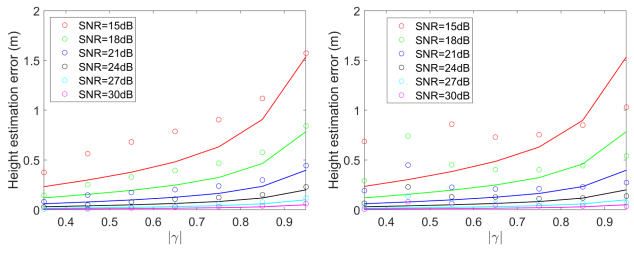

Fig. 24. Observed and theoretical errors as a function of the volume coherence with different SNRs. (a) First experiment. (b) Second experiment.

on the forest height estimation error under the given inversion workflow. There are two concerns remaining further analysis and discussion. First, there are two simplifications in the model derivation. Consequently, it should illustrate their influences and whether they can be expended. Second, whether the proposed error model remains valid for other inversion configurations as shown in Fig. 1.

Compared with the comprehensive TSI, there are two simplifications in the model derivation. The first simplification lies in the approximation of volume coherence. In the TSI, the volume coherence is obtained by the geometric characteristics of the RVoG model, namely, two coherence loci on the coherence region boundary with the largest distance [13]. As the volume coherence has no explicit analytic form, we estimate it by the phase diversity method, which provides a good approximation of the volume coherence as well as an analytic form. The second simplification is to fix the extinction as zero. Since the error model needs to solve the inverse of the inversion problem, the analysis is very difficult for a multivariate complex function, and fixing the extinction greatly simplifies the problem.

Two sets of comparative experiments are implemented to assess the impact of the two simplifications. Specifically, the first set of experiments replaced the PD method with two coherence loci on the coherence region boundary with the largest distance. The second set of experiments no longer fixed the extinction coefficient. Since the analysis has demonstrated that crosstalks and imbalance amplify the noise, the system is assumed as a noise-only system with different SNRs to facilitate the comparison.

Fig. 24 shows the theoretical errors versus the observed errors of the two sets of experiments with different SNRs. In the first set of experiments, the theoretical errors fit quite well with the observed errors compared with Fig. 10. It indicates that the errors introduced by the first simplification are minimal. In addition, the ML and MAP methods have been demonstrated equivalent to the TSI method for estimating ground phase and volume coherence [15]. Therefore, the proposed error model is also applicable to both methods under the first simplification. Nevertheless, the second set of experiments demonstrates that the influence of the second simplification is greater than that of the first.

In general, the proposed error model can accurately predict the height errors introduced by nonideal system parameters in different RVoG-based methods, including TSI, ML estimation, and MAP estimation. The major limitation is the simplification of extinction, which makes the model unsuitable in configurations where the extinction coefficient is not fixed.

VI. Conclusion

This study focuses on the impact of nonideal system parameters on the estimated forest height based on the RVoG model. The coupled effects of channel imbalance, crosstalk, and noise on the height estimation error are explicitly analyzed and derived. It indicates that the forest height estimation error is a multivariate function in terms of six physical parameters: the volume coherence γ_v, vertical wavenumber k_z, channel imbalance f, crosstalk δ_h, δ_v, and SNR. The channel imbalance, crosstalk, and SNR will lead to additional volume decorrelation, resulting in the overestimation of forest height. This study also shows how to design the system parameters and perform systematic error correction according to the proposed error model.

In addition, the retrieval errors inherent in the RVoG model may be higher than the random errors and biases introduced by nonideal system parameters for a well-designed PolInSAR system. Therefore, there are two critical points for the development of forest height estimation. On the one hand, well-designed spaceborne PolInSAR data are scarce and thus most of the studies are carried out in the airborne SAR data. On the other hand, there is an urgent need for more effective inversion models as existing models' accuracy is not good enough.

Appendix

To experimentally validate the performance of the proposed error model, we employed the other published model for comparison. The error model was proposed by Wang et al. [28] based on the two-layer model, and it integrated the Lagrange coherence optimization [29] and phase-amplitude joint method [30] (referred to as LPA). The forest height is estimated by

$$h_v = \frac{\phi_v - \phi_d}{k_z} + \varepsilon \frac{2\sin \mathrm{c}^{-1}\left(|\gamma_v|\right)}{k_z} \tag{41}$$

where ε is set to 0.4 [28]. The forest height error model is given by

$$\begin{aligned}\Delta h_v(|\widetilde{\gamma_1}|, \mathrm{SNR}, \delta, f, k_z) &= \frac{C}{k_z}\left(8.2|\widetilde{\gamma_1}|^3 - 6.9|\widetilde{\gamma_1}|^2 + 3|\widetilde{\gamma_1}|\right) \\ &\cdot \frac{1}{1+\mathrm{SNR}} \\ &\cdot \frac{1}{9}\left(\frac{1}{(1+\delta)^4} + \frac{1}{(1-\delta^2)^2} + \frac{1}{(1-\delta)^4}\right) \\ &\cdot \left(1 + \frac{1}{|f|^2} + \frac{1}{|f|^4}\right)\end{aligned} \tag{42}$$

where $C = 3.67$ is an empirical parameter. The detailed algorithm is referred to [28].

Acknowledgment

The authors would like to thank the European Space Agency (ESA) for providing the BioSAR 2008 dataset (ESA EO Project Campaign ID 69499).

REFERENCES

[1] W. Qi et al., "Improved forest height estimation by fusion of simulated gedi LiDAR data and TanDEM-X inSAR data," *Remote Sens. Environ.*, vol. 221, pp. 621–634, 2019.

[2] L. Alagialoglou, I. Manakos, M. Heurich, J. Červenka, and A. Delopoulos, "A learnable model with calibrated uncertainty quantification for estimating canopy height from spaceborne sequential imagery," *IEEE Trans. Geosci. Remote Sens.*, vol. 60, May 2022, Art. no. 4410913.

[3] L. Zhao, E. Chen, Z. Li, W. Zhang, and Y. Fan, "A new approach for forest height inversion using X-band single-pass inSAR coherence data," *IEEE Trans. Geosci. Remote Sens.*, vol. 60, Apr. 2021, Art. no. 5206018.

[4] K. P. Papathanassiou and S. R. Cloude, "Single-baseline polarimetric SAR interferometry," *IEEE Trans. Geosci. Remote Sens.*, vol. 39, no. 11, pp. 2352–2363, Nov. 2001.

[5] F. Garestier, P. C. Dubois-Fernandez, and I. Champion, "Forest height inversion using high-resolution P-band Pol-inSAR data," *IEEE Trans. Geosci. Remote Sens.*, vol. 46, no. 11, pp. 3544–3559, Nov. 2008.

[6] I. Hajnsek, F. Kugler, S. Lee, and K. P. Papathanassiou, "Tropical-forest-parameter estimation by means of Pol-inSAR: The INDREX-II campaign," *IEEE Trans. Geosci. Remote Sens.*, vol. 47, no. 2, pp. 481–493, Feb. 2009.

[7] F. Kugler, D. Schulze, I. Hajnsek, H. Pretzsch, and K. P. Papathanassiou, "TanDEM-X Pol-inSAR performance for forest height estimation," *IEEE Trans. Geosci. Remote Sens.*, vol. 52, no. 10, pp. 6404–6422, Oct. 2014.

[8] F. Kugler, S. Lee, I. Hajnsek, and K. P. Papathanassiou, "Forest height estimation by means of Pol-inSAR data inversion: The role of the vertical wavenumber," *IEEE Trans. Geosci. Remote Sens.*, vol. 53, no. 10, pp. 5294–5311, Oct. 2015.

[9] R. N. Treuhaft, S. N. Madsen, M. Moghaddam, and J. J. V. Zyl, "Vegetation characteristics and underlying topography from interferometric radar," *Radio Sci.*, vol. 31, no. 6, pp. 1449–1485, 1996.

[10] R. N. Treuhaft and P. R. Siqueira, "Vertical structure of vegetated land surfaces from interferometric and polarimetric radar," *Radio Sci.*, vol. 35, no. 1, pp. 141–177, 2000.

[11] S. Cloude and K. Papathanassiou, "Three-stage inversion process for polarimetric SAR interferometry," *IEE Proc.-Radar, Sonar Navigation*, vol. 150, no. 3, pp. 125–134, 2003.

[12] T. Mark, O. Jeffrey, F. Thomas, and C. Richard, "Phase diversity: A decomposition for vegetation parameter estimation using polarimetric SAR interferometry," in *Proc. Eur. Conf. Synthetic Aperture Radar, Conf. Proc.*, 2002, pp. 721–724.

[13] T. Flynn, M. Tabb, and R. Carande, "Coherence region shape extraction for vegetation parameter estimation in polarimetric SAR interferometry," in *Proc. IEEE Int. Geosci. Remote Sens. Symp.*, 2002, pp. 2596–2598.

[14] M. Tabb, T. Flynn, and R. Carande, "Full maximum likelihood inversion of polinsar scattering models," in *Proc. IEEE Int. Geosci. Remote Sens. Symp.*, 2004, pp. 1232–1235.

[15] Z. Huang, X. Lv, X. Li, and H. Chai, "Maximum a posteriori inversion for forest height estimation using spaceborne polarimetric SAR interferometry," *IEEE Trans. Geosci. Remote Sens.*, vol. 61, Jul. 2023, Art. no. 4406514.

[16] M. Neumann, L. Ferro-Famil, and A. Reigber, "Improvement of vegetation parameter retrieval from polarimetric SAR interferometry using a simple polarimetric scattering model," in *Proc. 4th POLinSAR Workshop*, Citeseer, 2009, pp. 1–9.

[17] M. Lavalle and S. Hensley, "Extraction of structural and dynamic properties of forests from polarimetric-interferometric SAR data affected by temporal decorrelation," *IEEE Trans. Geosci. Remote Sens.*, vol. 53, no. 9, pp. 4752–4767, Sep. 2015.

[18] M. García, S. Saatchi, S. Ustin, and H. Balzter, "Modelling forest canopy height by integrating airborne LiDAR samples with satellite radar and multispectral imagery," *Int. J. Appl. Earth Observ. Geoinformation*, vol. 66, pp. 159–173, 2018.

[19] W. Li, Z. Niu, R. Shang, Y. Qin, L. Wang, and H. Chen, "High-resolution mapping of forest canopy height using machine learning by coupling ICESat-2 LiDAR with sentinel-1, sentinel-2 and Landsat-8 data," *Int. J. Appl. Earth Observ. Geoinformation*, vol. 92, 2020, Art. no. 102163.

[20] M. Pourshamsi et al., "Tropical forest canopy height estimation from combined polarimetric SAR and LiDAR using machine-learning," *ISPRS J. Photogrammetry Remote Sens.*, vol. 172, pp. 79–94, 2021.

[21] A. E. Giraldez, "Saocom-1 Argentina l-band SAR mission overview," *ESA Special Pub.*, vol. 565, 2004, Art. no. 27.

[22] O. Montenbruck, G. Allende-Alba, J. Rosello, M. Tossaint, and F. Zangerl, "Precise orbit and baseline determination for the SAOCOM-CS bistatic radar mission," *Navigation: J. Inst. Navigation*, vol. 65, no. 1, pp. 15–24, 2018.

[23] H. Zhang et al., "End-to-end bistatic inSAR raw data simulation for TwinSAR-L mission," in *Proc. IEEE Int. Geosci. Remote Sens. Symp.*, 2019, pp. 3519–3522.

[24] T. L. Toan, "A P-band SAR for global forest biomass measurement: The biomass mission," in *Proc. XXXIth URSI Gen. Assem. Sci. Symp.*, 2014, pp. 1–2.

[25] A. Moreira et al., "Tandem-l: A highly innovative bistatic SAR mission for global observation of dynamic processes on the Earth's surface," *IEEE Geosci. Remote Sens. Mag.*, vol. 3, no. 2, pp. 8–23, Jun. 2015.

[26] Z. Huang, Y. Yun, H. Chai, and X. Lv, "The iterative extraction of the boundary of coherence region and iterative look-up table for forest height estimation using polarimetric interferometric synthetic aperture radar data," *Remote Sens.*, vol. 14, no. 10, 2022, Art. no. 2438.

[27] S. Cloude, "Calibration requirements for forest parameter estimation using polinsar," in *Proc. SAR Workshop Calibration/Validation*, 2003, Art. no. 19.

[28] X. Wang and F. Xu, "A polinsar inversion error model on polarimetric system parameters for forest height mapping," *IEEE Trans. Geosci. Remote Sens.*, vol. 57, no. 8, pp. 5669–5685, Aug. 2019.

[29] S. R. Cloude and K. P. Papathanassiou, "Polarimetric SAR interferometry," *IEEE Trans. Geosci. Remote Sens.*, vol. 36, no. 5, pp. 1551–1565, Sep. 1998.

[30] S. R. Cloude, "Polarization coherence tomography," *Radio Sci.*, vol. 41, no. 04, pp. 1–27, 2006.

[31] A. Ishimaru, "Multiple scattering theory of waves in stationary and moving scatterers and its relationship with transport theory," in *Proc. Wave Propag. Scattering Random Media*, 1997, pp. 245–286.

[32] S.-K. Lee, F. Kugler, K. Papathanassiou, and I. Hajnsek, "Multibaseline polarimetric SAR interferometry forest height inversion approaches," in *Proc. ESA POLinSAR Workshop*, 2011, pp. 1–7.

[33] E. W. Weisstein, "Series reversion," From MathWorld–A Wolfram Web Resource. Accessed: May 16, 2024. [Online]. Available: https://mathworld.wolfram.com/SeriesReversion.html

[34] D. W. Cantrell, "A series for the inverse sine cardinal function." Accessed: May 16, 2024. [Online]. Available: https://www.dsprelated.com/showthread/comp.dsp/13099-1.php

[35] J. J. Van Zyl, "Calibration of polarimetric radar images using only image parameters and trihedral corner reflector responses," *IEEE Trans. Geosci. Remote Sens.*, vol. 28, no. 3, pp. 337–348, May 1990.

[36] A. Freeman, J. J. Van Zyl, J. D. Klein, H. A. Zebker, and Y. Shen, "Calibration of stokes and scattering matrix format polarimetric SAR data," *IEEE Trans. Geosci. Remote Sens.*, vol. 30, no. 3, pp. 531–539, May 1992.

[37] S. Quegan, "A unified algorithm for phase and cross-talk calibration of polarimetric data-theory and observations," *IEEE Trans. Geosci. Remote Sens.*, vol. 32, no. 1, pp. 89–99, Jan. 1994.

[38] E. Warsitz and R. Haeb-Umbach, "Blind acoustic beamforming based on generalized eigenvalue decomposition," *IEEE Trans. audio, speech, Lang. Process.*, vol. 15, no. 5, pp. 1529–1539, Jul. 2007.

[39] H. Laudon et al., "Northern landscapes in transition: Evidence, approach and ways forward using the Krycklan catchment study," *Hydrological Processes*, vol. 35, no. 4, 2021, Art. no. e14170.

[40] H. Irena et al., "Biosar 2008 experiment final report," Report, 2009. Accessed: May 16, 2024. [Online]. Available: https://earth.esa.int/eogateway/documents/20142/37627/BIOSAR2_final_report.pdf

[41] S.-K. Lee, T. E. Fatoyinbo, D. Lagomasino, E. Feliciano, and C. Trettin, "Multibaseline TanDEM-X mangrove height estimation: The selection of the vertical wavenumber," *IEEE J. Sel. Topics Appl. Earth Observ. Remote Sens.*, vol. 11, no. 10, pp. 3434–3442, Oct. 2018.

Zenghui Huang received the B.S. degree in communication engineering from the College of Information and Communication Engineering, Harbin Engineering University, Harbin, China, in 2020. He is currently working toward the Ph.D. degree in signal processing with the Aerospace Information Research Institute, Chinese Academy of Sciences, Beijing, China.

He is currently with the University of Chinese Academy of Sciences, Beijing. His current research interests include polarimetric interferometric synthetic aperture radar and forest height inversion.

Xiaolei Lv (Member, IEEE) received the B.S. degree in computer science and technology and the Ph.D. degree in signal processing from Xidian University, Xi'an, China, in 2004 and 2009, respectively.

From 2009 to 2010, he was with the School of Electrical and Electronic Engineering, Nanyang Technological University, Singapore. From 2011 to 2013, he was with the Department of Civil and Environmental Engineering, Rensselaer Polytechnic Institute, Troy, NY, USA. Since 2013, he has been a Professor with the Aerospace Information Research Institute, Chinese Academy of Sciences, Beijing, China. His main research interests include sparse signal processing, radar imaging (synthetic aperture radar/inverse synthetic aperture radar), interferometric synthetic aperture radar, and ground moving-target indication.

Xiaoshuai Li received the B.S. degree in spatial information and digital technology from the College of Communication Engineering, Xidian University, Xi'an, China, in 2021. He is currently working toward the Ph.D. degree in signal processing with the Aerospace Information Research Institute, Chinese Academy of Sciences, Beijing, China.

He is currently with the University of Chinese Academy of Sciences, Beijing. His current research interests include polarimetric interferometric synthetic aperture radar and terrain inversion under forest.